rameters is given in Table I. The intensities were corrected for Lorentz and polarization effects. An empirical absorption correction using $\psi$ scans of $\chi - 90°$ reflections was employed.

Calculations were carried out with the SHELX system of computer programs.[15] Neutral atom scattering factors for Yb, N, C, and H were taken from ref 16, and the scattering was corrected for the real and imaginary components of anomalous dispersion.

The positions of the ytterbium atoms were revealed by using the direct methods program MULTAN. Difference Fourier maps phased on the ytterbium atoms revealed the positions of the non-hydrogen atoms. Two pyridine rings not associated with the ytterbium atoms were also located around centers of inversion. These rings were treated as completely disordered at each position (X in Table III) and refined as $^1/_6$ N and $^5/_6$ C.

Early in the data analysis, it appeared that the two independent molecules in the asymmetric unit were possibly symmetry related. An investigation of the positional parameters, space group, and final ORTEPs indicated that although the two molecules were mirror images of each other, the choice of space group ($P2_1/c$) was correct.

The size of the crystal used in this study and the large number of independent variables posed several problems in the refinement of the structure. Hence, the ytterbium atoms, coordinated nitrogen atoms, and the cyclooctatetraene carbon atoms were refined anisotropically, while the remaining carbon atoms were refined isotropically. The disordered pyridine rings were also refined isotropically. The hydrogen atom contributions were included in calculated positions (0.95 Å from the bonded carbon) for all but the uncoordinated pyridine rings and allowed to ride with $B$ fixed on the appropriate carbon atom. This refinement led to final values of $R = 0.062$ and $R_w = 0.081$. A final difference Fourier showed no feature greater than 1.2 e/Å$^3$. The weighting scheme was based on $[(1/\sigma_{F_o}{}^2) + (1/pF_o{}^2)]$ when $p = 0.0007$; no systematic variation of $w(|F_o| - |F_c|)$ vs. $|F_o|$ or $(\sin\theta)/\lambda$ was noted. The final values of the positional parameters are given in Table III.

**Acknowledgment.** R.D.R. wishes to thank the donors of the Petroleum Research Fund, administered by the American Chemical Society, and the NSF Chemical Instrumentation Program for partial support of this work. A.L.W. thanks Prof. T. Don Tilley for helpful discussions of pyridine purification procedures.

**Supplementary Material Available:** Tables of thermal parameters, bond distances and angles, least-squares planes, and H-atom fractional coordinates (8 pages); listings of structure factor amplitudes (10 pages). Ordering information is given on any current masthead page.

(15) Sheldrick, G. M., SHELX, a system of computer programs for X-ray structure determination as locally modified.
(16) *International Tables for X-Ray Crystallography*; Kynoch: Birmingham, England, 1972; Vol. IV, pp 72, 99, 149.
(17) Germain, G.; Main, P.; Woolfson, M. M. *Acta Crystallogr., Sect. A: Cryst. Phys., Diffr., Theor. Gen. Crystallogr.* **1971**, *A27*, 368.
(18) See paragraph at end of paper regarding supplementary material.

# Structural and Molecular Orbital Probes into the H/AuPR$_3$ Isolobal and Isostructural Analogy: $Fe_4(CO)_{12}(AuPPh_3)_2BH$ vs. $Fe_4(CO)_{12}BH_3$

Catherine E. Housecroft*†

*Department of Chemistry, University of New Hampshire, Durham, New Hampshire 03824*

Arnold L. Rheingold*

*Department of Chemistry, University of Delaware, Newark, Delaware 19716*

*Received October 20, 1986*

The preparation and crystal structure of the compound $Fe_4(CO)_{12}(AuPPh_3)_2BH$ are reported: triclinic, $P\bar{1}$, $a = 10.870$ (3) Å, $b = 12.114$ (3) Å, $c = 20.466$ (6) Å, $\alpha = 80.23$ (2)°, $\beta = 83.17$ (2)° $\gamma = 73.40$ (2)°, $V = 2537.9$ Å$^3$, $Z = 2$; $R_F = 4.49\%$. The new cluster is related to the known ferraborane $Fe_4(CO)_{12}BH_3$ by the replacement of two endo-hydrogen atoms by gold(I) triphenylphosphine units. However, the ferraborane and its aura derivative are not structurally analogous; the H/AuPR$_3$ substitution causes the "migration" of a hydrogen (in the form of AuPPh$_3$) from the metal framework toward the boron atom, thus causing the latter to be associated with six metal atoms. A boridic environment is therefore exemplified in the new cluster. Analysis of the molecular structure of $Fe_4(CO)_{12}(AuPPh_3)_2BH$ suggests that each AuPPh$_3$ unit is primarily associated with an iron–boron edge. Fenske–Hall calculations, which use CuPH$_3$ to model AuPPh$_3$, confirm the latter bonding description of the cluster. For $Fe_4(CO)_{12}BHX_2$ (X = H or CuPH$_3$), the preferences for a given isomer structure are examined within the framework of the Fenske–Hall calculations. The role played by the iron tricarbonyl units in "freezing" either a proton or an AuPR$_3^+$ unit into a particular site on the cluster surface is found to be significant. The isolobal analogy between H$^+$, CuPH$_3^+$, and AuPR$_3^+$ is supported by the results of the calculations even though $Fe_4(CO)_{12}BH_3$ and $Fe_4(CO)_{12}(AuPPh_3)_2BH$ are not structurally analogous.

The ability of the Lewis acid AuPR$_3^+$ to mimic H$^+$ through replacement in a transition-metal cluster is now well-established.[1-4] A few examples of H/AuPR$_3$ replacement in borane clusters are documented,[5] but the majority of examples of this isolobal relationship are found in transition-metal hydride cluster chemistry. Compounds in which one or more endo-hydrogen atoms have been replaced by gold fragments have been observed. When a single hydrogen atom is replaced, a structural analogy

† Present address: University Chemical Laboratory, Lensfield Road, Cambridge CB2 1EW, England.

(1) Lauher, J. W.; Wald, K. *J. Am. Chem. Soc.* **1981**, *103*, 7648.
(2) Bateman, L. W.; Green, M.; Mead, K. A.; Mills, R. M.; Salter, I. D.; Stone, F. G. A.; Woodward, P. *J. Chem. Soc., Dalton Trans.* **1983**, 2599.
(3) Hall, K. P.; Mingos, D. M. P. *Prog. Inorg. Chem.* **1984**, *32*, 237 and references therein.
(4) Horowitz, C. P.; Holt, E. M.; Brock, C. P.; Shriver, D. F. *J. Am. Chem. Soc.* **1985**, *107*, 8136 and references therein.

0276-7333/87/2306-1332$01.50/0 

between the transition-metal hydride or borane endo hydrogen and its gold derivative is usually apparent. Indeed, the structural characterization of aura-transition-metal cluster derivatives has been used as indirect evidence for the location of the analogous hydrogen atom in the parent transition-metal hydride.[6] Once the number of gold units is increased past one, the tendency for weak Au–Au interactions to develop becomes apparent[3] and the H/AuPR$_3$ structural analogy begins to show limitations. This is exemplified in the series $H_{3-x}(AuPPh_3)_xRu_3(CO)_9COMe$ ($x$ = 0–3).[2,7-9] Similarly, a comparison of $H_4Os_4(CO)_{12}$[10] with $H_2(AuPPh_3)_2Os_4(CO)_{12}$[11] shows that the gold units both bridge the same Os–Os edge and thus situate themselves within bonding contact rather than adopt the remote edge bridging sites of the corresponding hydrides. Interestingly, it is suggested[11] that a second isomer of $H_2(AuPPh_3)_2Os_4(CO)_{12}$, isolated but not structurally characterized, may be structurally analogous to its parent hydride. Recently, the characterization of $[Re_7C(CO)_{21}(AuPPh_3)]^{2-}$ has provided an example in which replacement of H by AuPPh$_3$ in a cluster leads to a preferential stabilization of one isomer: $[HRe_7C(CO)_{21}]^{2-}$ exhibits two isomers in solution whereas $[Re_7C(CO)_{21}(AuPPh_3)]^{2-}$ mimics only one of these.[12]

We report here $Fe_4(CO)_{12}(AuPPh_3)_2BH$[13] (I), which is the first example of a ferraborane in which endo-hydrogen atoms have been replaced by gold(I) triphenylphosphine units. The accompanying increased degree of metal–boron association that results as one of the hydrogen atoms "migrates" from the iron skeleton toward the boron in going from $HFe_4(CO)_{12}BH_2$[14,15] (II) to I allows I to be classified as a metal–boride cluster. Molecular orbital calculations, which use $CuPH_3$[16,17] to model AuPPh$_3$, are used to investigate the reasons for and the significance of this "proton migration". We illustrate that electrophile location is explicitly tied in with carbonyl ligand orientation. Moreover, we observe that the approaching electrophile ($H^+$ or $MPR_3^+$ (M = Au or Cu)), has to balance off strong overlap with the cluster core against resultant atomic charge.

## Experimental Section

**General Data.** FT-NMR spectra were recorded on a JEOL-90FXQ spectrometer; $^1$H NMR shifts are reported with respect to $\delta$ 0 for $Me_4Si$; $^{11}$B NMR with respect to $\delta$ 0 for $BF_3{\cdot}OEt_2$; $^{31}$P NMR with respect to $\delta$ 0 for $H_3PO_4$. Infrared spectra were recorded on a Perkin-Elmer 283B spectrometer or by using an FT-Nicolet 7199 instrument. Fast atom bombardment mass spectra were performed by the Midwest Center for Mass Spectrometry.

All reactions were carried out under nitrogen by using standard Schlenk techniques. Solvents (Fisher) were dried over molecular sieves, degassed, and, for diethyl ether and hexanes, distilled from sodium/benzophenone before use. $AuPPh_3Cl$ (Aldrich) and 60–200 mesh silica gel (Baker) were used as received.

**Preparation of I.** $[HFe_4(CO)_{12}BH]PPN$[18] (PPN = bis(triphenylphosphine)nitrogen(1+)) (0.04 mmol) in $CH_2Cl_2$ (4 mL) was added to an excess of solid $AuPPh_3Cl$ at room temperature with stirring. After 30 min, solvent was removed and the product extracted from PPNCl and excess $AuPPh_3Cl$ with 4 × 3 mL aliquots of diethyl ether. Compound I was the major product and was the first band (brown-green) after elution with hexanes/$CH_2Cl_2$ (1:2) on a silica gel column. Removal of solvent from the fraction gave a brown-green solid that was moderately air-sensitive. I: 28.7-MHz $^{11}$B NMR ($(CD_3)_2CO$, 20 °C) $\delta$ 141.3 (br s, fwhm = 185 Hz, {$^1$H} fwhm = 110 Hz, $J_{BH} \simeq$ 90 Hz); 89.5-MHz $^1$H NMR ($(CD_3)_2CO$, 20 °C) $\delta$ 7.57–7.25 (m, 30 H, Ph), –9.1 (br, 1 H, FeHB); 36.2-MHz $^{31}$P NMR ($(CD_3)_2CO$, –70 °C) $\delta$ 53.0; IR ($CH_2Cl_2$, cm$^{-1}$) $\nu_{CO}$ 2056 (m), 2009 (vs), 1996 (vs), 1967 (m), 1925 (sh); FAB-MS in MNBA matrix, $m/z$ 1490 ($P^+$).

**X-ray Structural Determination of I.** Experimental parameters are collected in Table I. A green-black specimen obtained by recrystallization from $CH_2Cl_2$ layered with hexane was mounted on a glass fiber; preliminary photographic characterization revealed no crystal symmetry higher than triclinic. Data collection extended to the $2\theta$ limits of availability. A linear decay of ~4% was observed, and corrections were made. An empirical absorption correction using 252 data refined and a six-parameter pseudoellipsoid model reduced $R$(int) for these data from 14.8 to 3.9%. The centrosymmetric space group, $P\bar{1}$, was assumed initially and later proved correct by the computationally stable and chemically rational results of refinement.

A three-dimensional Patterson synthesis provided the Au atom locations, and the remaining, non-hydrogen atoms were located from subsequent difference Fourier syntheses. All non-hydrogen

**Table I. Crystal Data for $Fe_4(CO)_{12}\{Au(PPh_3)\}_2BH$**

(a) Crystal Parameters

| | | | |
|---|---|---|---|
| formula | $C_{48}H_{31}Au_2Fe_4P_2O_{12}$ | $\gamma$, deg | 73.40 (2) |
| cryst system | triclinic | $V$, Å$^3$ | 2537.9 |
| space group | $P\bar{1}$ | $Z$ | 2 |
| $a$, Å | 10.870 (3)[a] | $D$(calcd), g cm$^{-3}$ | 1.949 |
| $b$, Å | 12.114 (3) | $\mu$(Mo K$\alpha$), cm$^{-1}$ | 70.2 |
| $c$, Å | 20.466 (6) | cryst color | green-black |
| $\alpha$, deg | 80.23 (2) | cryst size, mm | 0.24 × 0.30 × 0.37 |
| $\beta$, deg | 83.17 (2) | temp, K | 294 |

(b) Data Collection

| | | | |
|---|---|---|---|
| diffractometer | Nicolet R3m/$\mu$ | reflns collected | 8320 |
| radiatn | Mo K$\alpha$ | unique rflns | 7942 |
| wavelength, Å | $\lambda$ = 0.71073 | unique rflns ($3\sigma(F_o)$) | 5474 |
| monochromator | graphite | $R$(int), % | 1.20 |
| scan method | Wyckoff | $T_{max}/T_{min}$ | 2.23 |
| scan limits, deg | $4 \le 2\theta \le 48$ | std rflns | 3 std/197 rflns |
| scan speed, deg min$^{-1}$ | var 5–20 | decay | linear, 4% |

(c) Refinement

| | | | |
|---|---|---|---|
| $R(F)$,$R(wF)$, % | 4.49, 5.20 | $\Delta(\rho)_{max}$, e Å$^{-3}$ | 1.13 |
| GOF | 1.102 | $N_o/N_v$ | 10.0 |
| $\Delta/\sigma$ | 0.08 | $g$; $w^{-1}=\sigma^2(F_o)+gF_o^2$ | 0.001 |

[a] Least-squares best fit of the angular settings of 25 reflections ($22° \le 2\theta \le 29°$).

(5) Wynd, A. J.; Robins, S. E.; Welch, D. A.; Welch, A. J. *J. Chem. Soc., Chem. Commun.* **1985**, 819. Beckett, M. A.; Crook, J. E.; Greenwood, N. N.; Kennedy, J. D. *J. Chem. Soc., Dalton Trans.* **1984**, 1427.
(6) (a) As reported in ref 1. (b) Halpin, C. F.; Hall, M. B. *J. Am. Chem. Soc.* **1986**, *108*, 1695.
(7) Farrugia, L. J.; Freeman, M. J.; Green, M.; Orpen, A. G.; Stone, F. G. A.; Salter, I. D. *J. Organomet. Chem.* **1983**, *249*, 273.
(8) Hodali, H. A.; Shriver, D. F. *Inorg. Chem.* **1979**, *18*, 1236.
(9) Keister, J. B.; *J. Chem. Soc., Chem. Commun.* **1979**, 214.
(10) Johnson, B. F. G.; Lewis, J.; Raithby, P. R.; Zuccaro, C. *Acta Crystallogr., Sect. B: Struct. Crystallogr. Cryst. Chem.* **1981**, *B37*, 1728.
(11) Johnson, B. F. G.; Kaner, D. A.; Lewis, J.; Raithby, P. R.; Taylor, M. *Polyhedron* **1982**, *1*, 105.
(12) Henley, T. J.; Shapley, J. R.; Rheingold, A. L. *J. Organomet. Chem.* **1986**, *310*, 55.
(13) A preliminary report has appeared: Housecroft, C. E.; Rheingold, A. L. *J. Am. Chem. Soc.* **1986**, *108*, 6420.
(14) Wong, K. S.; Scheidt, W. R.; Fehlner, T. P. *J. Am. Chem. Soc.* **1982**, *104*, 1111.
(15) Fehlner, T. P.; Housecroft, C. E.; Scheidt, W. R.; Wong, K. S. *Organometallics* **1983**, *2*, 825.
(16) $PH_3$ has been shown to represent a justifiable model for $PPh_3$: Kostic, N. M.; Fenske, R. F. *Organometallics* **1982**, *1*, 489.
(17) Since basis functions for Au were not available for the Fenske–Hall calculations, Cu was substituted for Au. Our calculations deal with a comparison of proton vs. heavy metal based electrophile, and qualitative conclusions made for Cu will be valid for Au. Quantitative results for Au should show the same trends as those obtained for Cu, and a comparison of $AuPR_3$ vs. H should follow trends observed for $CuPH_3$ vs. H.
(18) Housecroft, C. E.; Fehlner, T. P. *Organometallics* **1986**, *5*, 379.

**Table II. Atomic Coordinates (×10⁴) and Isotropic Thermal Parameters (Å² × 10³)**

| | x | y | z | U[a] |
|---|---|---|---|---|
| Au(1) | 1016.0 (4) | 3248.7 (4) | 1902.8 (2) | 42 (1) |
| Au(2) | 2932.8 (4) | 2464.8 (3) | 2903.5 (1) | 38 (1) |
| Fe(1) | -806 (1) | 4619 (1) | 2592 (1) | 39 (1) |
| Fe(2) | 1641 (1) | 4652 (1) | 2731 (1) | 37 (1) |
| Fe(3) | -677 (2) | 2692 (1) | 3467 (1) | 42 (1) |
| Fe(4) | -134 (2) | 4539 (1) | 3769 (1) | 44 (1) |
| P(1) | 1668 (3) | 2316 (2) | 981 (2) | 40 (1) |
| P(2) | 4523 (3) | 738 (2) | 3048 (2) | 38 (1) |
| B | 727 (11) | 3418 (10) | 3046 (6) | 33 (4) |
| C(1) | -770 (12) | 5632 (11) | 1883 (8) | 66 (6) |
| O(1) | -757 (12) | 6313 (10) | 1404 (6) | 110 (6) |
| C(2) | -1867 (13) | 4102 (10) | 2222 (7) | 62 (5) |
| O(2) | -2643 (10) | 3819 (8) | 1989 (6) | 88 (5) |
| C(3) | 902 (12) | 6176 (10) | 2591 (7) | 56 (5) |
| O(3) | 560 (9) | 7177 (7) | 2497 (5) | 80 (4) |
| C(4) | 2686 (14) | 4717 (10) | 2005 (7) | 63 (6) |
| O(4) | 3396 (11) | 4883 (9) | 1560 (6) | 101 (6) |
| C(5) | 2800 (12) | 4648 (9) | 3279 (7) | 53 (5) |
| O(5) | 3537 (10) | 4699 (8) | 3618 (6) | 86 (5) |
| C(6) | -781 (11) | 1572 (10) | 2768 (6) | 85 (5) |
| O(6) | -821 (10) | 825 (8) | 2768 (6) | 85 (5) |
| C(7) | -426 (11) | 1862 (10) | 4271 (7) | 51 (5) |
| O(7) | -241 (10) | 1333 (9) | 4789 (5) | 87 (5) |
| C(8) | -2386 (13) | 3251 (10) | 3602 (7) | 56 (5) |
| O(8) | -3485 (9) | 3587 (9) | 3698 (6) | 99 (5) |
| C(9) | -1459 (12) | 4517 (11) | 4380 (6) | 61 (5) |
| O(9) | -2235 (10) | 4555 (9) | 4804 (5) | 91 (5) |
| C(10) | 1065 (12) | 3655 (11) | 4302 (6) | 52 (5) |
| O(10) | 1810 (9) | 3110 (9) | 4651 (5) | 79 (4) |
| C(11) | -61 (12) | 5917 (11) | 3918 (7) | 60 (5) |
| O(11) | -43 (11) | 6817 (9) | 4032 (6) | 98 (6) |
| C(12) | -1828 (12) | 5647 (10) | 3062 (7) | 60 (5) |
| O(12) | -2680 (10) | 6418 (9) | 3235 (6) | 103 (5) |
| C(21) | -615 (7) | 3507 (6) | 394 (4) | 60 (5) |
| C(22) | -1580 | 3669 | -33 | 68 (6) |
| C(23) | -1568 | 2791 | -397 | 65 (6) |
| C(24) | -590 | 1751 | -335 | 70 (6) |
| C(25) | 376 | 1589 | 92 | 61 (6) |
| C(26) | 363 | 2467 | 456 | 41 (4) |
| C(31) | 3370 (8) | 209 (6) | 700 (4) | 71 (6) |
| C(32) | 3898 | -993 | 825 | 79 (7) |
| C(33) | 3445 | -1638 | 1385 | 72 (7) |
| C(34) | 2465 | -1081 | 1819 | 88 (8) |
| C(35) | 1937 | 121 | 1693 | 72 (6) |
| C(36) | 2390 | 766 | 1133 | 40 (4) |
| C(41) | 2680 (6) | 3301 (6) | -239 (4) | 53 (5) |
| C(42) | 3603 | 3761 | -635 | 69 (6) |
| C(43) | 4711 | 3785 | -363 | 66 (6) |
| C(44) | 4897 | 3348 | 304 | 69 (6) |
| C(45) | 3974 | 2888 | 700 | 58 (5) |
| C(46) | 2866 | 2864 | 428 | 42 (4) |
| C(51) | 6255 (8) | 1388 (6) | 2082 (4) | 58 (5) |
| C(52) | 7134 | 1282 | 1525 | 75 (7) |
| C(53) | 7379 | 314 | 1195 | 98 (9) |
| C(54) | 6747 | -547 | 1422 | 124 (10) |
| C(55) | 5869 | -441 | 1979 | 83 (7) |
| C(56) | 5623 | 526 | 2308 | 47 (4) |
| C(61) | 6768 (7) | -121 (7) | 3734 (4) | 62 (5) |
| C(62) | 7502 | -224 | 4267 | 85 (7) |
| C(63) | 7009 | 448 | 4777 | 83 (8) |
| C(64) | 5782 | 1223 | 4754 | 87 (8) |
| C(65) | 5048 | 1325 | 4221 | 57 (5) |
| C(66) | 5541 | 653 | 3711 | 46 (5) |
| C(71) | 2543 (6) | -340 (5) | 3382 (4) | 52 (5) |
| C(72) | 2023 | -1275 | 3613 | 65 (6) |
| C(73) | 2835 | -2394 | 3759 | 65 (6) |
| C(74) | 4167 | -2577 | 3674 | 69 (6) |
| C(75) | 4687 | -1642 | 3443 | 61 (5) |
| C(76) | 3875 | -524 | 3297 | 46 (4) |

[a] Equivalent isotropic $U$ defined as one-third of the trace of the orthogonalized $U_{ij}$ tensor.

atoms were refined anisotropically; hydrogen atoms were incorporated as idealized, isotropic, updated contributions (the H atom on B was ignored). The phenyl rings were treated as rigid, planar hexagons with $d$(C–H) = 1.395 Å.

**Table III. Selected Distances (Å) and Angles (deg) from I**

(a) Bond Distances (Å)

| | | | |
|---|---|---|---|
| Au(1)-Au(2) | 2.943 (1) | Fe(4)-C(12) | 2.42 (1) |
| Au(1)-Fe(1) | 2.630 (1) | Au(1)-B | 2.36 (1) |
| Au(1)-Fe(2) | 2.852 (2) | Au(2)-B | 2.35 (1) |
| Au(2)-Fe(2) | 2.606 (1) | Fe(1)-B | 2.07 (1) |
| Fe(1)-Fe(2) | 2.720 (2) | Fe(2)-B | 2.00 (1) |
| Fe(1)-Fe(3) | 2.671 (2) | Fe(3)-B | 2.01 (1) |
| Fe(1)-Fe(4) | 2.578 (2) | Fe(4)-B | 2.13 (1) |
| Fe(2)-Fe(4) | 2.708 (2) | Au(1)-P(1) | 2.299 (3) |
| Fe(3)-Fe(4) | 2.655 (3) | Au(2)-P(2) | 2.302 (2) |
| Fe(1)-C(12) | 1.75 (1) | | |

(b) Bond Angles (deg)

| | | | |
|---|---|---|---|
| P(1)-Au(1)-Au(2) | 112.3 (1) | Au(2)-Fe(2)-B | 59.7 (3) |
| P(2)-Au(2)-Au(1) | 128.3 (1) | Au(2)-B-Fe(1) | 144.4 (5) |
| P(1)-Au(1)-Fe(1) | 149.3 (1) | Au(2)-B-Fe(2) | 73.0 (4) |
| P(1)-Au(1)-Fe(2) | 145.3 (1) | Au(2)-B-Fe(3) | 126.6 (5) |
| P(1)-Au(1)-B | 156.4 (3) | Au(2)-B-Fe(4) | 125.5 (6) |
| P(2)-Au(2)-Fe(2) | 164.9 (1) | Fe(1)-Fe(2)-Fe(4) | 56.7 (1) |
| P(2)-Au(2)-B | 147.0 (3) | Fe(1)-Fe(2)-B | 49.1 (3) |
| Au(1)-Au(2)-B | 51.4 (3) | Fe(1)-Fe(3)-Fe(4) | 57.9 (1) |
| Au(1)-Au(2)-Fe(2) | 61.5 (0) | Fe(1)-Fe(3)-B | 50.1 (3) |
| Au(2)-Au(1)-B | 51.2 (3) | Fe(1)-Fe(4)-Fe(2) | 61.9 (1) |
| Au(2)-Au(1)-Fe(1) | 98.0 (0) | Fe(1)-Fe(4)-Fe(3) | 61.3 (1) |
| Au(2)-Au(1)-Fe(2) | 53.4 (0) | Fe(1)-Fe(4)-B | 51.1 (3) |
| Au(1)-Fe(1)-B | 58.8 (3) | Fe(1)-B-Fe(2) | 83.8 (4) |
| Au(1)-Fe(1)-Fe(2) | 64.4 (0) | Fe(1)-B-Fe(3) | 81.8 (5) |
| Au(1)-Fe(1)-Fe(3) | 84.4 (1) | Fe(1)-B-Fe(4) | 75.7 (4) |
| Au(1)-Fe(1)-Fe(4) | 110.8 (1) | Fe(2)-Fe(1)-Fe(3) | 94.0 (1) |
| Au(1)-Fe(2)-B | 54.8 (3) | Fe(2)-Fe(1)-Fe(4) | 61.4 (1) |
| Au(1)-Fe(2)-Fe(1) | 56.3 (0) | Fe(2)-Fe(1)-B | 47.0 (4) |
| Au(1)-Fe(2)-Fe(4) | 100.8 (1) | Fe(2)-Fe(4)-Fe(1) | 61.9 (1) |
| Au(1)-B-Au(2) | 77.3 (3) | Fe(2)-Fe(4)-Fe(3) | 97.7 ( 1) |
| Au(1)-B-Fe(1) | 72.5 (4) | Fe(2)-B-Fe(3) | 158.9 (6) |
| Au(1)-B-Fe(2) | 81.3 (4) | Fe(2)-B-Fe(4) | 81.8 (5) |
| Au(1)-B-Fe(3) | 108.8 (6) | Fe(3)-Fe(1)-Fe(4) | 60.7 (1) |
| Au(1)-B-Fe(4) | 145.3 (5) | Fe(3)-Fe(1)-B | 48.2 (3) |
| Au(2)-Fe(2)-Au(1) | 65.1 (0) | Fe(3)-Fe(4)-B | 48.2 (4) |
| Au(2)-Fe(2)-Fe(1) | 104.4 (1) | Fe(4)-Fe(3)-B | 52.1 (3) |
| Au(2)-Fe(2)-Fe(4) | 97.2 (1) | | |

**Chart I**

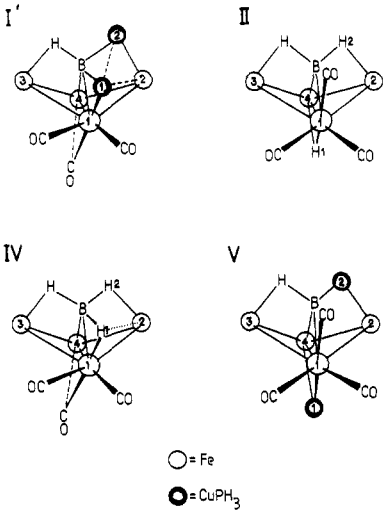


All programs are contained in the SHELXTL program library (Nicolet Corp., Madison, WI). Atomic coordinates are provided in Table II, and selected bond distances and angles in Table III. Additional crystallographic data are available in the microfilm edition of ref 13.

**Calculations.** Fenske–Hall[19] and extended Hückel[20] calculations were carried out on the compound $Fe_4(CO)_{12}BHX_2$ (X =

(19) Hall, M. B.; Fenske, R. F. *Inorg. Chem.* **1972**, *11*, 768.
(20) Hoffmann, R. *J. Chem. Phys.* **1963**, *39*, 1397.

**Table IV. Extended Hückel Parameters**

| atom | orbital | Slater exponent | $H_{ii}$, eV | ref |
|---|---|---|---|---|
| H | 1s | 1.3 | −13.60 | 24 |
| B | 2s | 1.3 | −14.01 | 25 |
| | 2p | 1.3 | −8.28 | |
| C | 2s | 1.625 | −21.40 | 24 |
| | 2p | 1.625 | −11.40 | |
| O | 2s | 2.275 | −32.30 | 24 |
| | 2p | 2.275 | −14.80 | |
| Fe | 3d | 2.60 | −11.67 | 24 |
| | 4s | 0.97 | −9.75 | |
| | 4p | 0.97 | −5.99 | |
| Cu | 3d | 2.83 | −14.00 | 26 |
| | 4s | 2.20 | −11.40 | |
| | 4p | 2.20 | −6.06 | |
| P | 3s | 1.60 | −18.60 | 27 |
| | 3p | 1.60 | −14.00 | |

H or $CuPH_3$) in structures I′, II, IV, and V defined in Chart I. Structure I′ is based on I with $CuPH_3$ units replacing $AuPPh_3$ units. Structure IV is based on the structure of I with X = H. Structures II and V are derived from the crystallographically determined structure of II with idealized $C_{2v}$ symmetry for the $Fe_4(CO)_{12}$ core. The internal dihedral angle of the tetrairon butterfly was constant at 114° in each compound (see text). The hinge Fe(1)–Fe(4) bond was 2.62 Å when bridged and 2.58 Å when unbridged. All C–O bonds were set at 1.13 Å, and Fe–CO bonds were 1.80 Å. In I′ and V, the boron atom was 0.37 Å above the Fe(2)–Fe(3) axis; in II and IV, the boron atom was 0.31 Å above this axis. Bond distances: I′, B–Cu(1) = 2.33, B–Cu(2) = 2.31, Fe(1)–Cu(1) = 2.53, Fe(2)–Cu(2) = 2.58, Fe(2)–Cu(1) = 2.81, Cu(1)–Cu(2) = 2.67 Å; II and IV, B–H(2) = 1.37, Fe(2)–H(2) = 1.56 Å; II, Fe(1)–H(1) = Fe(4)–H(1) = 1.66 Å; IV, Fe(1)–H(1) = 1.59, B–H(1) = 1.38, Fe(2)···H(1) = 2.18 Å; V, B–Cu(2) = 2.10, Fe(2)–Cu(2) = 2.56, Fe(1)–Cu(1) = Fe(4)–Cu(1) = 2.56 Å. In each case, the environment around Fe(1) was kept close to octahedral. For $CuPH_3$: Cu–P = 2.21, P–H = 1.41 Å.

The Fenske-Hall basis functions for Fe, C, B, O, and H were as previously reported.[21] The Cu functions were chosen for the +1 oxidation state and were taken from the results of Richardson.[22] They were single-$\zeta$ except for the 3d functions which were double-$\zeta$; the 4s and 4p functions were chosen to be 2.0. For P, "best atom" functions[23] were employed. The extended Hückel calculations employed Slater functions, and the orbital exponents and diagonal matrix elements used are given in Table IV. The arithmetic mean Wolfsberg–Helmholz approximation with $K$ = 1.75 was used.

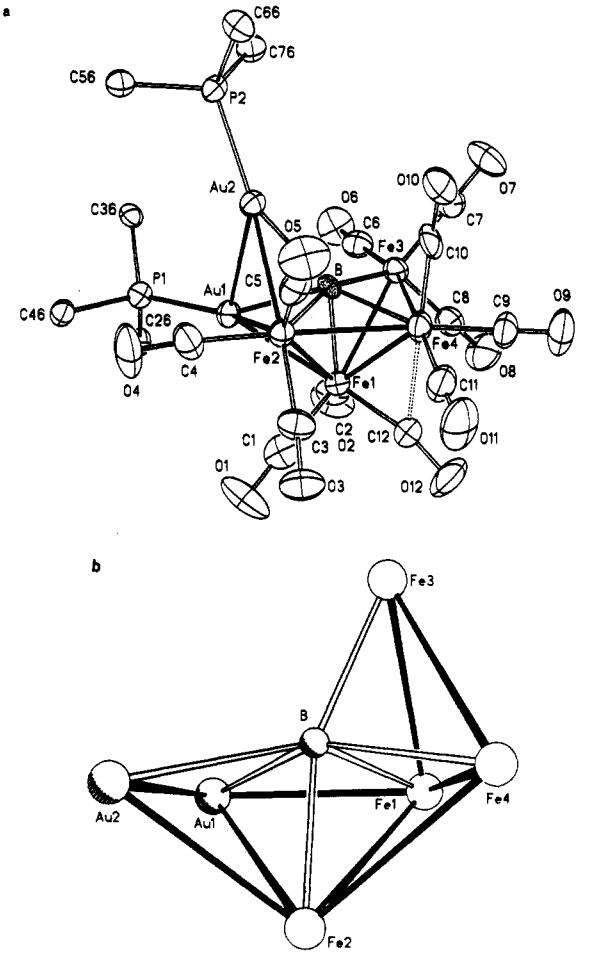


**Figure 1.** (a) Molecular structure and labeling scheme for I. Phenyl rings are depicted as ipso-carbon atoms only. (b) The $Fe_4Au_2B$ cluster core structure of I.

## Results and Discussion

**Molecular Structure of I.** The molecular structure of I is shown in Figure 1a, and pertinent bond length and bond angle data are listed in Table III. The metal cluster core (Figure 1b) exhibits the same tetrairon butterfly arrangement present both in the precursor $[HFe_4(CO)_{12}BH]^-$ and its conjugate acid II, the structure of which has previously been determined and the hydrogen atoms located.[14] A stereoview of I is shown in Figure 2. The spatial array of the four iron atoms shows little change in going from II to I: the internal dihedral angle of the fragment changes from 114.0° in II to 113.4° in I. The hinge bond, Fe(1)–Fe(4), shortens 0.059 Å as the bridging hydrogen atom, present in II but not in I, is removed. The wing of the iron butterfly that is associated with the two $AuPPh_3$ units exhibits slightly longer Fe–Fe bonds than those in the other wing. Bonds in the latter show negligible differences compared to the wingtip-hinge Fe–Fe bonds in II. The boron atom in I is situated 0.37 Å above the butterfly wingtip axis in I (compared to 0.31 Å in II) and is skewed toward hinge atom Fe(1), presumably as a consequence of the interaction of the boron atom with Au(1). The positions of the $AuPPh_3$ units may be viewed in one of two ways. First, Au(1) may be described as capping the Fe(1)Fe(2)B face with Au(2) capping the Fe(2)Au(1)B face.[13] However, careful inspection of the bond lengths listed in Table III shows that two of the Au–Fe contacts contrast with the third: that is, Fe(1)–Au(1) and Fe(2)–Au(2) are 2.630 (1) and 2.606 (1) Å, respectively, while Fe(2)–Au(1) is noticeably longer (2.852 (2) Å). Table V summarizes Fe–Au bond distances for structurally characterized iron–

(21) Housecroft, C. E. *J. Organomet. Chem.* **1984**, *276*, 297. Housecroft, C. E.; Fehlner, T. P. *Organometallics* **1984**, *3*, 764.
(22) Richardson, J. W.; Nieuwpoort, W. C., Powell, R. R.; Edgell, W. F. *J. Chem. Phys.* **1962**, *36*, 1057.
(23) Clementi, E.; Raimondi, D. L. *J. Chem. Phys.* **1963**, *38*, 2686.
(24) Burdett, J. K. *J. Chem. Soc., Dalton Trans.* **1977**, 424.
(25) Basch, H.; Viste, A.; Gray, H. B. *Theor. Chim. Acta* **1964**, *3*, 458.
(26) From double-$\zeta$ functions of: Hoffmann, R.; Summerville, R. *J. Am. Chem. Soc.* **1976**, *98*, 7240.
(27) Albright, T. A.; Hoffmann, R.; Thibeault, J. C.; Thorn, D. L. *J. Am. Chem. Soc.* **1979**, *101*, 3801.
(28) Arndt, L. W.; Darensbourg, M. Y.; Fackler, J. P., Jr.; Lusk, R. J.; Marler, D. O.; Youngdahl, K. A. *J. Am. Chem. Soc.* **1985**, *107*, 7218.
(29) Lauher, J. W., reported in ref 3.
(30) Briant, C. E.; Hall, K. P.; Mingos, D. M. P. *J. Chem. Soc., Chem. Commun.* **1983**, 843.
(31) Fischer, K.; Muller, M.; Vahrenkamp, H. *Angew. Chem., Int. Ed. Engl.* **1984**, *23*, 140.
(32) Bruce, M. I.; Nicholson, B. K. *J. Organomet. Chem.* **1983**, *250*, 627.
(33) Johnson, B. F. G.; Kaner, D. A.; Lewis, J.; Rosales, M. J. *J. Organomet. Chem.* **1982**, *238*, C73.
(34) Roland, E.; Fischer, K.; Vahrenkamp, H. *Angew. Chem., Int. Ed. Engl.* **1983**, *22*, 326.
(35) Johnson, B. F. G.; Kaner, D. A.; Lewis, J.; Raithby, P. R.; Rosales, M. J. *J. Organomet. Chem.* **1982**, *231*, C59.
(36) Andrianov, V. G.; Struchkov, Y. T.; Rossinskaja, E. R. *J. Chem. Soc., Chem. Commun.* **1973**, 338.

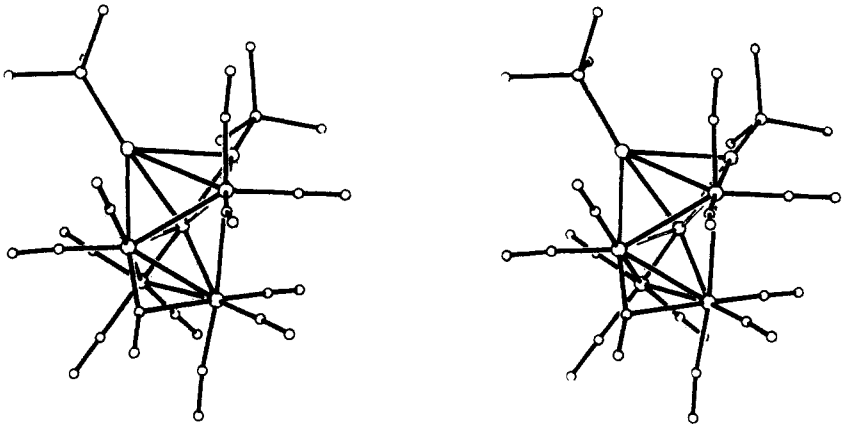

**Figure 2.** Stereoview of I. The butterfly wing Fe(1)Fe(2)Fe(4) is in the foreground.

**Table V. Comparative Fe–Au Bond Lengths as a Function of Bonding Environment**

| compound | *d*(Fe–Au), Å | environment[a] | ref |
|---|---|---|---|
| $(CO)_5WFe(CO)_4(AuPPh_3)$ | 2.520 (3) | 2c-2e | 28 |
| $(CO)_4Fe(AuPPh_3)_2$ | 2.545 (1) | 2c-2e | 29 |
| $[Fe(CO)_4Au_2(dppm)]_2$ | 2.608 (3), 2.539 (3) | $FeAu_2$ triangle | 30 |
| $[Fe(CO)_4Au_2(dppe)]_2$ | 2.524 (2), 2.535 (2) | $FeAu_2$ triangle | 30 |
| $[Fe_4(CO)_{13}(AuPEt_3)]^-$ | 2.666 (1) | FeAuFe bridge | 4 |
| $Fe_4(CO)_{12}(AuPEt_3)COCH_3$ | 2.666 (2), 2.675 (3) | FeAuFe bridge | 4 |
| $FeRuCo(CO)_9(AuPPh_3)(PMe)$ | 2.677 (2) | FeAuRu bridge | 31 |
| $Fe_3(CO)_9(\mu_3\text{-}HC{=}N\text{-}t\text{-}Bu)(AuPPh_3)$[b] | (i) 2.671 (3), 2.679 (3) | FeAuFe bridge | 32 |
| | (ii) 2.659 (2), 2.717 (3) | FeAuFe bridge | |
| $Fe_5(CO)_{14}C(AuPEt_3)_2$ | 2.696 (2), 2.701 (3) | FeAuFe bridge | 33 |
| | 2.828 (3), 3.007 (2), 3.036 (3), 2.871 (2) | multicenter | |
| $Fe_3(CO)_9(AuPPh_3)_2S$ | 2.722 (3), 2.698 (4), 2.746 (3), 2.671 (3), 2.750 (4) | multicenter | 34 |
| $HFe_4(CO)_{12}C(AuPPh_3)$ | 2.854 (1), 2.880 (1) | multicenter | 35 |
| $Fe_4(CO)_{12}C(AuPEt_3)_2$ | 2.770 (1), 2.982 (2), 2.999 (2) | multicenter | 35 |
| $[(\eta\text{-}C_5H_5)Fe(\eta\text{-}C_5H_4)(AuPPh_3)_2]^+$ | 2.818 (9) | multicenter | 36 |

[a] 2c-2e = 2-center 2-electron. [b] Two crystallographically independent molecules.

gold containing compounds. The data illustrate the distinction between 2-center 2-electron, 3-center 2-electron, and multicenter cluster bonds in which the iron and gold atoms are counted as vertices of polyhedra. Comparing these data with the Fe–Au bond lengths in I, Fe(1)–Au(1) and Fe(2)–Au(2) appear to fall into the category of 3-center bonds, while Fe(2)–Au(1) appears to be a part of a multicenter bonding array. Both Au–B bonds are similar: 2.36 (1) and 2.35 (1) Å. Thus, a consideration of structural parameters suggests that each $AuPPh_3$ unit is primarily associated with an iron–boron edge and that secondary Au(1)–Fe(2) and Au(1)–Au(2) interactions exist to stabilize the structure. In terms of the isolobal analogy, $Au(2)PPh_3$ in I can be considered structurally analogous to the Fe(2)–H–B proton in II. Au(2) bridges the Fe(2)–B edge in I as does H(2) in II, although interaction of Au(2) with Au(1) in I causes a slight distortion of Au(2) off the plane containing Fe(2), Fe(3), and the midpoint of the Fe(1)–Fe(4) bond. $Au(1)PPh_3$ in I, however, is clearly not structurally analogous to the hinge-bridging hydride, H(1), in II. Instead, replacement of H by gold(I) has caused a "migration" of the hydride, now in the guise of gold triphenylphosphine, from the base of the iron butterfly toward the boron atom. It is worth noting that in the anion $[HFe_4(CO)_{12}BH]^-$, the two endo-hydrogens that bridge Fe(1)–Fe(4) and Fe(2)–B, respectively, are fluxional at room temperature on the 300-MHz $^1H$ NMR time scale,[18,37] and therefore migration of an endo-hydrogen atom between metal framework and metal–boron associated sites obviously takes place. The mechanism of scrambling, however, has not been elucidated. In II, the endo-hydrogen atoms are static at room temperature.[14] The net result of the "hydrogen atom migration" upon replacement by $AuPPh_3$ is the almost complete encapsulation of the boron atom by metal atoms. Thus, I exemplifies a metal boride environment.[13] A related "proton migration" is observed in a comparison[13] of the structures of $HFe_4(CO)_{12}CH$[38] and $Fe_4(CO)_{12}C(AuPEt_3)_2$.[35]

The carbonyl orientations in I are interesting. The $Fe(CO)_3$ fragments at Fe(2), Fe(3), and Fe(4) show no particular perturbation in going from the all protonated II to the aura derivative I. However, the iron tricarbonyl unit on Fe(1) is twisted through approximately 60°, bringing the axial carbonyl C(12)O(12) into a semibridging position (Figure 1). This location was occupied by the hinge-bridging hydride in II. The C(12)Fe(1) bond vector points almost directly at Au(1), thus providing Fe(1) with a near octahedral environment (angle Au(1)Fe(1)C(12) = 174.5°). The significance of the carbonyl reorientation in going from II to I is considered in the calculational section.

Although in I, the endo-hydrogen atom was not located crystallographically, the $^1H$ NMR shift of −9.1 ppm (i.e., close to that in $[HFe_4(CO)_{12}BH]^-$[18] and in II[14]) and observed coupling to boron indicate that it bridges an Fe–B edge, probably Fe(2)–B by analogy with II. Thus, the octahedral environment of Fe(3) would be completed.

Finally, $Au(1)PPh_3$ and $Au(2)PPh_3$ are not equivalent (Figure 1), and yet, in the $^{31}P$ NMR spectrum, a single resonance is observed even at the lowest temperature studied (−70 °C). Assuming an intramolecular process, the site equivalence of the phosphorus atoms can be ration-

(37) Housecroft, C. E.; Fehlner, T. P. *Organometallics* **1986**, *5*, 1279.

(38) Beno, M. A.; Williams, J. M.; Tachikawa, M.; Muetterties, E. L. *J. Am. Chem. Soc.* **1981**, *103*, 1485.

(39) Kostic, N. M.; Fenske, R. F. *Organometallics* **1982**, *1*, 974.

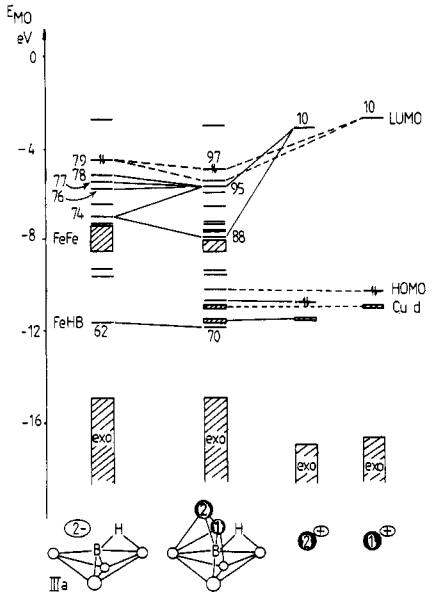


**Figure 3.** Correlation diagram for the formation of I′ from the three fragments IIIa, Cu(1)PH$_3^+$, and Cu(2)PH$_3^+$. Continuous correlation lines refer to interactions of IIIa with Cu(2), and dotted lines refer to interactions of IIIa with Cu(1). Fragment MO energies are taken from the Fock matrix.[39]

**Chart II**

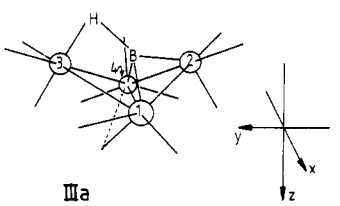


alized by a "rocking" motion of the [Au(PPh$_3$)]$_2$ unit across the Fe(2)–B bond,[13] thus exchanging the gold units between the two types of site. The only concurrent requirement for this process is the continual reorientation of the tricarbonyl units on iron atoms 1 and 4. Although we have not studied the $^{13}$C NMR spectrum of I, it is not at all unreasonable to anticipate facile localized CO site exchange.

**Electronic Structure of I.** By using the model compound Fe$_4$(CO)$_{12}$(CuPH$_3$)$_2$BH with CuPH$_3$ units replacing the AuPPh$_3$ units in I, the electronic structure of I is analyzed in terms of the interactions of the two CuPH$_3^+$ fragments with a tetrairon butterfly fragment, [Fe$_4$(CO)$_{12}$BH]$^{2-}$ (IIIa) (Chart II). Cu(2) interacts with the free Fe(wing)–B edge. Cu(1) is brought in to interact with Fe(1), B, Cu(2), and Fe(2) in a manner that mimics the interaction of Au(1) with the rest of the cluster in I; the distance Fe(1)–Cu(1) is shorter than Fe(2)–Cu(1). A correlation diagram for the interactions of the three fragments is drawn in Figure 3, and Mulliken overlap populations for the major interactions are listed in Table VI. As expected,[40] the lowest unoccupied molecular orbital (LUMO) of each electrophile (i.e., the empty sp-hybrid orbital on copper) is the principal orbital responsible for binding each unit to the cluster. The HOMO, lower lying copper-containing MO's, and exo-PH bonding MO's of each CuPH$_3^+$ are carried across unperturbed to the complex (Figure 3).

The LUMO of Cu(2)PH$_3^+$ interacts with MO's 74, 76, 77, and 78 of IIIa (Table VI) giving rise to two bonding

(40) Evans, D. G.; Mingos, D. M. P. *J. Organomet. Chem.* **1982**, *232*, 171.

**Table VI. Mulliken Overlap Populations between the Fragments IIIa, Cu(1)PH$_3^+$, and Cu(2)PH$_3^+$ in I′**

| IIIa fragment MO | Cu(1)PH$_3^+$ LUMO (MO 10) | Cu(2)PH$_3^+$ LUMO (MO 10) |
|---|---|---|
| 79 (HOMO) | 0.147 | |
| 78 | 0.011 | 0.068 |
| 77 | 0.012 | 0.042 |
| 76 | 0.013 | |
| 74 | 0.023 | 0.127 |
| total Mulliken overlap pop. between fragments | 0.206 | 0.244 |

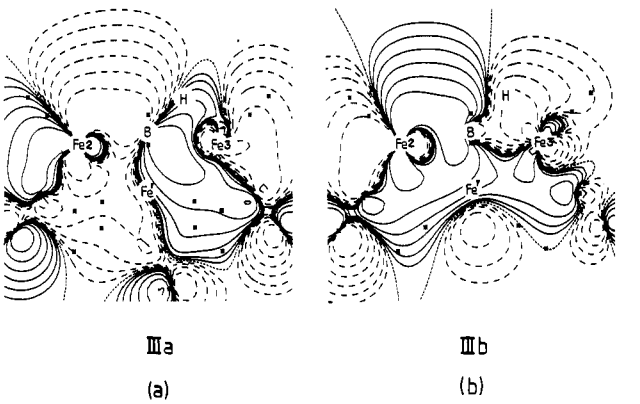


**Figure 4.** Amplitude contour plots for MO 74 in (a) IIIa and (b) IIIb. The plots are in the *yz* plane containing Fe(2), Fe(3), H, and B; Fe′ is the midpoint of the Fe(1)–Fe(4) bond; all other atoms are projected onto the plane and are represented by asterisks. The largest contour is 0.05 electron au$^{-3}$, and each succeeding contour differs from the last by a factor of 2.

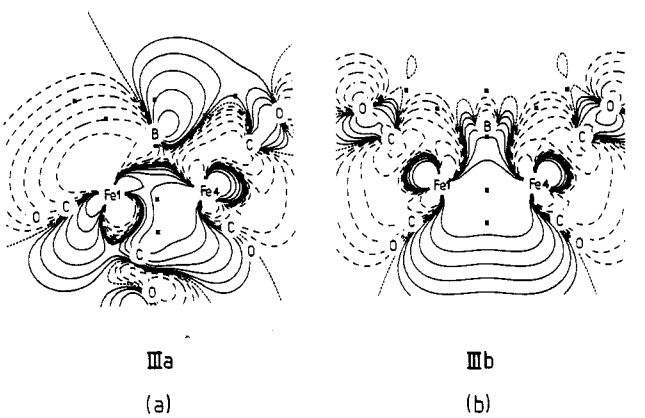


**Figure 5.** Amplitude contour plots for the HOMO (MO 79) in (a) IIIa and (b) IIIb. The plots are in the *xz* plane containing Fe(1), Fe(4), and B; CO ligands on the hinge iron atoms are projected onto the *xz* plane; other atoms are projected onto the plane and are indicated by asterisks. The largest contour is 0.05 electron au$^{-3}$, and each succeeding contour differs from the last by a factor of 2.

MO's (88 and 95) in the complex. MO 74 of IIIa is shown in Figure 4a. The region of Lewis basicity located between Fe(2) and the boron atom is apparent, and it is easy to envision the evolution of a 3-center Fe(2)–Cu(2)–B interaction as the CuPH$_3^+$ fragment approaches.

Cu(1) is bound in I′ primarily via the interaction of the LUMO of Cu(1)PH$_3^+$ with the HOMO of IIIa. Seventy-one percent of the total Mulliken overlap population between these two fragments is found in this single interaction; the other 29% is spread through a number of minor interactions (Table VI). The HOMO of IIIa is shown in Figure 5a. Note the outward pointing spd-hybrid orbital centered on hinge iron atom Fe(1) and also the Fe(1)–B bonding character of the MO. This orbital is ideally suited

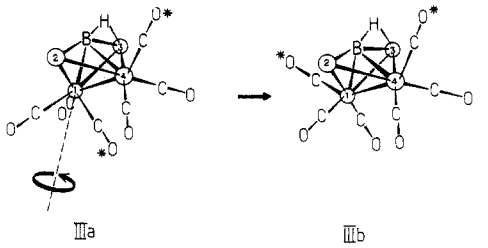


**Figure 6.** Structures of the fragment $[Fe_4(CO)_{12}BH]^{2-}$: IIIa exhibits the carbonyl orientations as found experimentally in I, and IIIb has carbonyl orientations as found in II. The CO's labeled with asterisks are those which are opposite to a vacant octahedral site ("axial" CO). Carbonyl ligands on wingtip atoms Fe(2) and Fe(3) have the same orientations in IIIa and IIIb and have been omitted from the diagram for clarity.

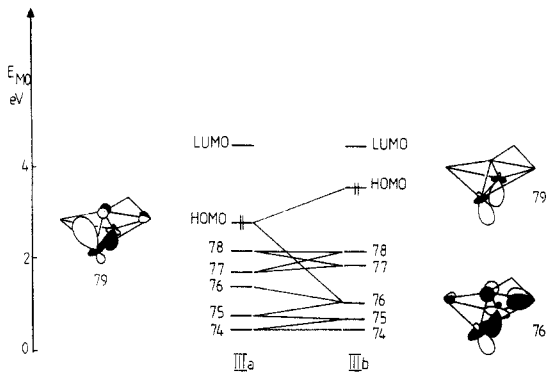


**Figure 7.** Correlation diagram of the frontier MO's of IIIa and IIIb. The HOMO of IIIa and its derivative MO's in IIIb are represented schematically.

for interaction with an electrophile. The dominant role of the HOMO in binding Cu(1) in I′ (and by analogy Au(1) in I) is reflected in the molecular structure of I; viz., experimental bond distance data suggest primary Fe(1)–Au(1) and B–Au(1) interactions.

**Diprotonation of IIIb to II.** The electronic structure of II has previously been presented in terms of a $[HFe_4(CO)_{12}]^+$ fragment interacting with a $BH_2^-$ ligand.[15] In order to gain some insight into the similarities and differences between the electronic structures of I and II and, most significantly, the analogy between a proton and an $AuPR_3^+$ or $CuPR_3^+$ unit interacting with the $[Fe_4(CO)_{12}BH]^{2-}$ cluster anion, an analysis of the diprotonation of IIIb to generate II follows.

Fragment IIIb differs from IIIa only in that the carbonyl ligands on hinge atom Fe(1) are reoriented (Figure 6) and the Fe(1)–Fe(4) bond is lengthened. In IIIb, the $Fe(CO)_3$ units on Fe(1) and Fe(4) are related by a mirror plane passing through Fe(2), Fe(3), and B, whereas in IIIa they are not. The frontier orbitals in IIIb are derived from those in IIIa as indicated in Figure 7, and emphasis is given to the rehybridization of the HOMO.

A correlation diagram for the interaction of two $H^+$ with IIIb to give II is shown in Figure 8, and Mulliken overlap populations for the major interactions are listed in Table VII. $H(1)^+$ interacts primarily with the HOMO (Figure 5b) of IIIb to generate the Fe(1)–H–Fe(4) bridging MO 64 in II. $H(2)^+$ interacts with frontier MO's 74, 75, and 78 and with the lower lying MO 63, all of which exhibit Fe(wing)–B bonding character. MO 74 is depicted in Figure 4b. Since the energy of the $H^+$ 1s orbital is significantly lower than the LUMO of $CuPH_3^+$[41] with respect to the

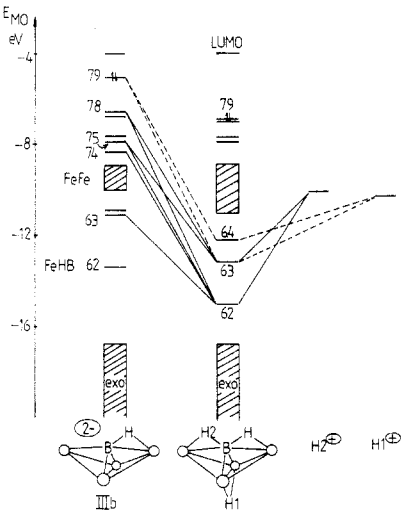


**Figure 8.** Correlation diagram for the formation of II from the three fragments IIIb, $H(1)^+$, and $H(2)^+$. Continuous correlation lines refer to the interactions of $H(2)^+$ with IIIb, and dotted lines refer to the interactions of $H(1)^+$ with IIIb. Fragment MO energies are taken from the Fock matrix.[39]

**Table VII. Mulliken Overlap Populations between the Fragments IIIb, $H(1)^+$, and $H(2)^+$ in II**

| fragment MO in IIIb | $H(1)^+$ 1s AO | $H(2)^+$ 1s AO |
|---|---|---|
| 79 (HOMO) | 0.312 | |
| 78 | | 0.122 |
| 75 | | 0.067 |
| 74 | | 0.096 |
| 63 | | 0.053 |
| total Mulliken overlap pop. between fragments | 0.312 | 0.338 |

fragment MO's of $[Fe_4(CO)_{12}BH]^{2-}$ (Figure 3 vs. Figure 8), it is not surprising that, in binding to the Fe(2)–B edge, $H(2)^+$ incorporates an interaction with MO 63 of IIIb whereas there is no corresponding significant interaction for Cu(2) interacting with IIIa. This is in spite of the fact that MO 63 in IIIa is strongly Fe(2)–B bonding. Apart from this and taking into account the correlations made in Figure 7, we observe that $H(2)^+$ and $Cu(2)PH_3^+$ interact with the Fe(2)–B edge of $[Fe_4(CO)_{12}BH]^{2-}$ in analogous manners. Thus, the isolobal analogy holds well for this particular interaction. In comparing the interactions of $H(1)^+$ and $Cu(1)PH_3^+$ with IIIb and IIIa, respectively, we observe that, although there is a significant structural difference between the final complexes II and I′, the interactions are similar; the HOMO of the cluster anion is, in each case, the predominant bonding MO, and the two HOMO's are obviously derived from each other (Figure 7). Thus, a comparison of the HOMO's of IIIa and IIIb follows.

Each hinge iron atom in IIIa and IIIb exhibits a single vacancy in an otherwise octahedral environment. Hoffmann[42] has presented the simple, but useful, concept that, for example, a square-pyramidal $ML_5$ unit possesses a frontier orbital set comprising the metal $t_{2g}$ set plus a hybrid orbital pointing toward the vacant octahedral ligand site. Indeed, this is exactly what we see in the $[Fe_4(CO)_{12}BH]^{2-}$ fragment, and it is clearly illustrated in Figure 5.

In both IIIa and IIIb, the HOMO (which, remember, controls the binding of H(1) or Cu(1)) is comprised of contributions from the two hinge iron atoms. Their hybrid

(41) The LUMO of $AuPPh_3^+$ will be higher still. A comparison of $CuPH_3$ and $AuPH_3$ MO's is given in ref 40.

(42) Hoffmann, R. (Nobel Lecture) *Angew. Chem., Int. Ed. Engl.* **1982**, *21*, 711.

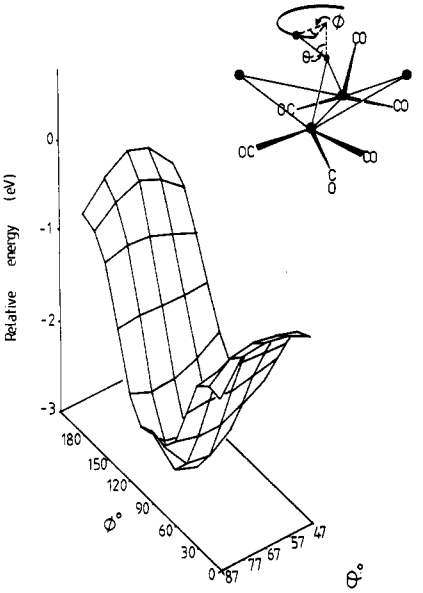


**Figure 9.** Extended Hückel potential energy surface calculated by using the total energy of filled MO's in IIIa and plotted as a function of endo-hydrogen atom position. The rotation angle and tilt angle are defined in the figure and text.

orbitals point outwards and opposite to the axial carbonyl ligands that are marked with asterisks in Figure 6. In IIIb, these hybrid orbitals constructively interfere (Figure 5b) providing a site for electrophilic attack along the Fe(1)–Fe(4) edge. This is the case for protonating IIIb. This feature has previously been observed for the interaction of the cluster carbide anion $[Fe_4(CO)_{12}C]^{2-}$ with electrophiles.[43,44] In IIIa, the hinge $Fe(CO)_3$ units are no longer symmetrically disposed with respect to the midpoint of the Fe(1)–Fe(4) bond, and the approaching electrophile will encounter a nodal plane between Fe(1) and Fe(4). Figure 5a shows that the hybrid orbital on Fe(4) is clearly a residual from the pair of inward pointing orbitals depicted in Figure 5b. The hybrid on Fe(1), however, now points to the upper side of the cluster and, moreover, has a positive overlap with a $2p_x$ orbital located on the boron atom and parallel to the Fe(1)–Fe(4) edge. An electrophile approaching IIIa will therefore tend to be associated with the Fe(1)–B edge. This is observed in going from IIIa to I′ or to I. Thus, we emphasize that the electrophile location and the carbonyl orientation are mutually dependent.

Another way of observing the consequences of reorienting the hinge iron tricarbonyl units on stabilizing electrophile location is to construct a potential energy surface for the movement of the endo-hydrogen atom in IIIa over the upper surface of the cluster. Figure 9 illustrates the variation in extended Hückel total energy of the filled MO's in IIIa as the hydrogen atom is moved according to the scheme shown in the inset in Figure 9. Rotation through an angle $\phi$ describes a semicircular path beginning above Fe(4) and ending above Fe(1). (Remember that Fe(1) and Fe(4) are distinct by virtue of their respective carbonyl ligand orientations.) Rotation through an angle $\theta$ tilts the B–H bond vector bringing the hydrogen atom closer to the metal framework as $\theta$ is increased; the starting angle of $\theta = 47°$ is the experimental position for an Fe(wing)–H–B bridge hydrogen atom in II,[14] and the final angle of $\theta = 87°$ provides a reasonable Fe(hinge)–H–B location for the hydrogen atom when $\phi = 0°$. Two important features are apparent in Figure 9. First, bridging an Fe(wing)–B edge is energetically more favorable than bridging an Fe(hinge)–B edge. Secondly, however, it is obvious that the change in orientation of the carbonyl ligands about Fe(1) makes a significant difference to the likelihood of the endo-hydrogen atom adopting an Fe(hinge)–H–B bridge position. The point corresponding to a Fe(1)–H–B bridge is actually the second minimum on the potential energy surface. In the light of the discussion above, this result is expected: the proton will be stabilized by the presence of an orbital pointing outwards from the metallaborone framework.

**Table VIII. Mulliken Overlap Populations between the Fragments IIIb, Cu(1)$PH_3^+$, and Cu(2)$PH_3^+$ in V**

| fragment MO in IIIb | Cu(1)$PH_3^+$ LUMO | Cu(2)$PH_3^+$ LUMO |
|---|---|---|
| 79 (HOMO) | 0.263 | |
| 78 | | 0.121 |
| 75 | | 0.061 |
| 74 | | 0.057 |
| 63 | | 0.013 |
| total Mulliken overlap pop. between fragments | 0.263 | 0.252 |

**Table IX. Mulliken Overlap Populations between the Fragments IIIa, H(1)$^+$, and H(2)$^+$ in IV**

| fragment MO in IIIa | H(1)$^+$ 1s AO | H(2)$^+$ 1s AO |
|---|---|---|
| 79 (HOMO) | 0.127 | |
| 78 | 0.010 | 0.065 |
| 77 | | 0.052 |
| 76 | 0.032 | |
| 75 | | 0.036 |
| 74 | 0.017 | 0.122 |
| 64 | 0.039 | |
| 63 | | 0.047 |
| total Mulliken overlap pop. between fragments | 0.225 | 0.322 |

**H$^+$ Location vs. CuPH$_3^+$ or AuPPh$_3^+$ Location.** So far, we have presented the idea that in II and I′, respectively, H(2) and Cu(2) are bound in analogous fashions to the Fe(wing)–B edge. In addition, given that the hinge $Fe(1)(CO)_3$ unit is free to reorient itself (a process that is reasonable in view of the facile localized site exchange undergone by many transition-metal carbonyl systems) an electrophile can interact either with the Fe(1)–Fe(4) or the Fe(1)–B edge. In each case, the interaction is governed by the HOMO of the cluster anion, and therefore interaction of IIIa with Cu(1) and IIIb with H(1) may be considered partly analogous. Why is it then that I is not structurally analogous to II? (The answer does not lie in steric reasons, since $[Fe_4(CO)_{13}(AuPR_3)]^-$ (R = Et, Ph) exists with $AuPR_3$ in a hinge-bridging position.[4]) This question may be answered by comparing two isomers for each system: I′ is compared with V, and II is compared with IV (Chart I). In terms of the isolobal principle, IV is structurally analogous to I′ and II is analogous to V. Mulliken overlap populations for the interactions of IIIb with $2CuPH_3^+$ units to form V and for IIIa combining with $2H^+$ to give IV are listed in Tables VIII and IX, respectively. First, compare the formation of isomers I′ and V (Tables VI and VIII). The Mulliken overlap populations point toward isomer V being preferred over I′ rather than the opposite as observed experimentally in I. Cu(1) has 28% enhanced overlap population with the cluster fragment in V compared to I′, while Cu(2) gains only marginally. For protons interacting with $[Fe_4(CO)_{12}BH]^{2-}$, the preference for bridging the Fe(1)–Fe(4) hinge bond is again predicted by comparing the overlap populations in Tables VII and IX; there is a marginal gain in overlap for the

(43) Wijeysekera, S. D.; Hoffmann, R.; Wilker, C. N. *Organometallics* **1984**, *3*, 962.
(44) Harris, S.; Bradley, J. S. *Organometallics* **1984**, *3*, 1086.

**Table X. Mulliken Charges on X in $Fe_4(CO)_{12}BHX_2$**

| compd | | Mulliken charges[a] X(1)[b] | X(2)[c] |
|---|---|---|---|
| X = $CuPH_3$ | I′ | 0.474 | 0.552 |
| | | (0.124) | (0.186) |
| | V | 0.300 | 0.583 |
| | | (−0.075) | (0.230) |
| X = H | II | −0.317 | −0.033 |
| | IV | −0.099 | −0.034 |

[a] The charge in parentheses is the Cu *atomic* charge. [b] Hinge-associated atom. [c] Wing-associated atom.

Fe(wing)–H–B hydrogen atom and a substantial (39%) gain for the hinge associated proton in going from isomer IV to II. That is, the Mulliken overlap populations correctly predict the relative stabilities of the isomers considered for $Fe_4(CO)_{12}BH_3$.

Consider now the Mulliken charges for $Fe_4(CO)_{12}BHX_2$ that are listed in Table X. For X associated with a Fe(wing)–B bridge site, isomerism for IV to II or from I′ to V results in only a small change in the charge transferred from the cluster fragment to X. For X = Cu(2)$PH_3$, the copper atom remains positively charged in both isomers. However, on relocating the electrophile from the Fe(1)–B to the Fe(1)–Fe(4) bridging position, a substantial increase in negative charge buildup on X occurs. For X = Cu(1)-$PH_3$, this results in the copper atom actually attaining an overall negative charge, a situation that is presumably not tolerated by the metal. However, for X = H(1), the amphoteric nature of the hydrogen atom will allow tolerance of the hydridic environment. Thus we see the electrophile striving for maximum overlap with the cluster anion, but at the same time, being influenced by the atomic charge as a function of environment. $Fe_4(CO)_{12}BH_3$ will be stable as isomer II. Calculations on the model $Fe_4(CO)_{12}(CuPH_3)_2BH$ indicate structure I′ will persist, as indeed is observed experimentally for I.

**Acknowledgment.** The experimental work was supported under a grant from Research Corp. which is gratefully acknowledged. NSF provided support for the purchase of the University of Delaware's diffractometer. Mass spectrometric determinations were performed by the Midwest Center for Mass Spectrometry, an NSF Regional Instrumentation Facility (Grant No. CHE-8211164). C. E.H. thanks the University of Notre Dame for hospitality shown to her as a guest research associate and the Computing Center there for computing time. The aid of R. Barreto and F.-E. Hong with the calculations is also gratefully acknowledged.

**Supplementary Material Available:** Table 1S, atomic coordinates, Table 2S, bond distances, Table 3S, bond angles, Table 4S, anisotropic temperature factors, and Table 5S, hydrogen atom coordinates (8 pages); Table 6S, observed and calculated structure factors (33 pages). Ordering information is given on any current masthead page.